ADVANCED MATERIALS
www.advmat.de

Optoelectronic Devices for In-Sensor Computing

*Qinqi Ren, Chaoyi Zhu, Sijie Ma, Zhaoqing Wang, Jianmin Yan, Tianqing Wan, Weicheng Yan, and Yang Chai**

The demand for accurate perception of the physical world leads to a dramatic increase in sensory nodes. However, the transmission of massive and unstructured sensory data from sensors to computing units poses great challenges in terms of power-efficiency, transmission bandwidth, data storage, time latency, and security. To efficiently process massive sensory data, it is crucial to achieve data compression and structuring at the sensory terminals. In-sensor computing integrates perception, memory, and processing functions within sensors, enabling sensory terminals to perform data compression and data structuring. Here, vision sensors are adopted as an example and discuss the functions of electronic, optical, and optoelectronic hardware for visual processing. Particularly, hardware implementations of optoelectronic devices for in-sensor visual processing that can compress and structure multidimensional vision information are examined. The underlying resistive switching mechanisms of volatile/nonvolatile optoelectronic devices and their processing operations are explored. Finally, a perspective on the future development of optoelectronic devices for in-sensor computing is provided.

1. Introduction

The accurate and reliable understanding of the physical world relies heavily on the deployment of abundant sensors. The demand for precise perception has driven the dramatic increase in sensory nodes, which are estimated to be increase from 40 billion in 2022 to 450 trillion by 2032.[1,2] By 2032, it is projected that the volume of data generated from sensors will escalate to $\approx 10^{27}$ bytes per year, which is equivalent to processing data at a rate surpassing 10^{20} bits per second.[3] At sensory terminals, abundant data are crucial to achieve accuracy, precision, and reliability; at computation terminals, large volumes of data delays in computing speed. This dilemma arises from the inherent tension between data richness and computational efficiency.

In addition, the raw data obtained directly from multiple sensors in the noisy analogue domain is often unstructured, which lacks a predefined format or organization and does not conform to a specific data model. To process these massive and unstructured sensory data, conventional sensory computing systems have to transfer the data from sensory terminals to local computation units or cloud-based systems (**Figure 1a**), which inevitably poses great challenges in terms of power-efficiency, transmission bandwidth, data storage, time latency, and security.[4–8] Therefore, it has become quite necessary to perform data compression and structuring at sensory terminals.

Data compression serves the purpose of minimizing data storage space or transmission bandwidth by using short representations to retain the essential information. The data compression ratio (C) represents the reduction from "data bits" to "information bits," as described in Equation (1)

$$C = \frac{\text{Data Bits}}{\text{Information Bits}} \tag{1}$$

Under this definition, data are the medium to convey information. To tackle the escalating sensory data growth, it is crucial to realize elevated C values within sensors, thus demanding the computational sensors to compress the sensory data. In classical information theory, information entropy quantifies the inherent randomness in a dataset, establishing a minimum number of bits needed to encode sensory information.[9] The information entropy $H(X)$ of event X represents the sum of the information content ($-\log_2 P(X_i)$) of each possible value X_i multiplied by its probability $P(X_i)$, as specified in Equation (2)

$$H(X) = -\sum_{i=1}^{n} P(x_i) \log_2 P(x_i) \tag{2}$$

The definition of information content reflects the expectation that events with high probabilities convey less information. $H(X)$ reflects the level of information compression achieved, denotes the minimum data necessary to fully describe information without distortion. Hence, encoding information with less than $H(X)$

Q. Ren, C. Zhu, S. Ma, Z. Wang, J. Yan, T. Wan, W. Yan, Y. Chai
Department of Applied Physics
The Hong Kong Polytechnic University
Kowloon, Hong Kong 999077, China
E-mail: ychai@polyu.edu.hk

Q. Ren, C. Zhu, S. Ma, Z. Wang, J. Yan, T. Wan, W. Yan, Y. Chai
Joint Research Centre of Microelectronics
The Hong Kong Polytechnic University
Kowloon, Hong Kong 999077, China

The ORCID identification number(s) for the author(s) of this article can be found under https://doi.org/10.1002/adma.202407476

DOI: 10.1002/adma.202407476

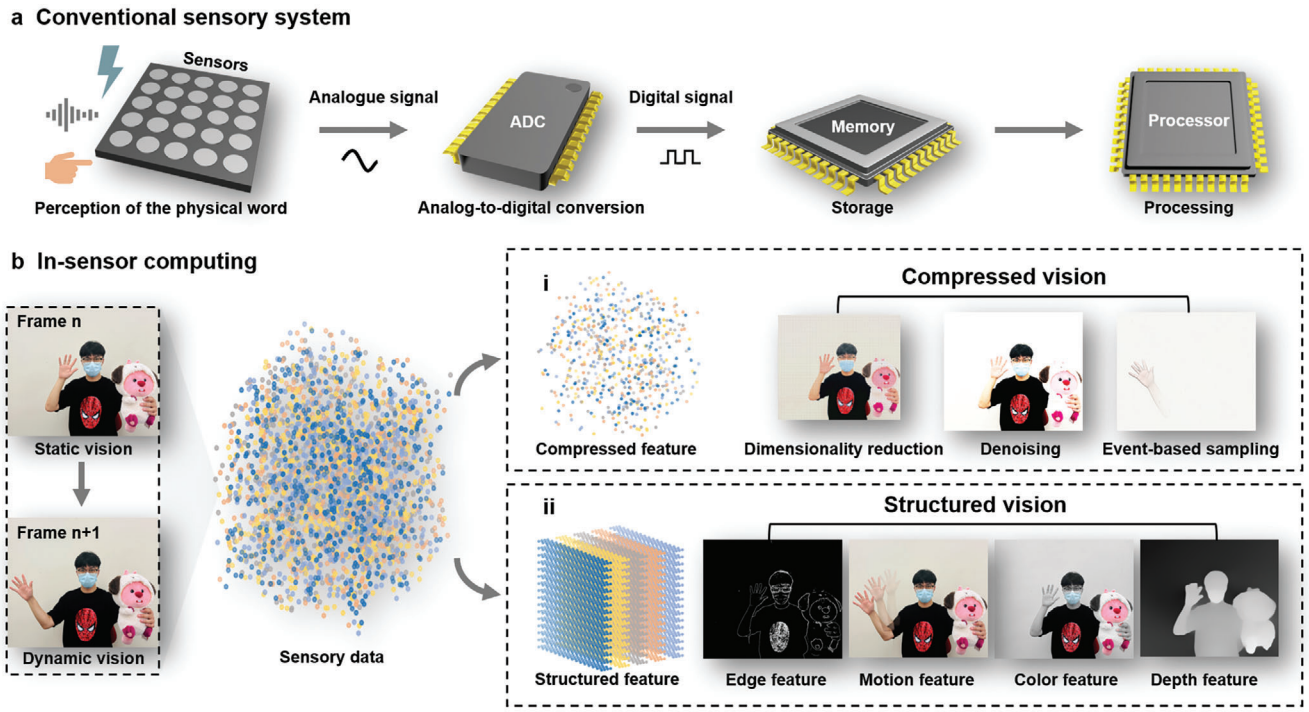

Figure 1. In-sensor computing for data compression and structuring. a) The architecture of the conventional sensory system. External stimuli are detected by multiple sensors, then converted into digital signals through analog-to-digital conversion, stored in memory, and finally processed by processors. b) Vision sensors can perform in-situ compression of sensory data, such as i) dimensionality reduction, denoising, and event-based sampling, as well as transforming visual data into structured features including ii) edges, motion, color, and depth.

bits of entropy is impossible. Furthermore, $H(X)$ directly impacts detection accuracy and certainty. The higher $H(X)$ indicates greater uncertainty in the detected information due to data redundancy. In-sensor computing can efficiently compress data at sensory terminals by eliminating randomness and unnecessary details, resulting in decreased information entropy and improved data robustness.[10] For example, vision compression involves dimensionality reduction, denoising, and event-driven sampling (Figure 1b,i). Notably, biological sensory system is quite efficient for data compression. They receive data at ≈10 M bits s^{-1}, but can consciously process information less than 50 bits s^{-1}, achieving the C of ≈200 000:1.[11,12]

Data structuring involves organizing raw data into a more systematic and manageable form, extracting key features. Data structuring often involves a degree of data compression, in which redundant information is discarded during the extraction of key features, facilitating more direct data analysis. The Hadamard product refers to the element-wise product operation of two matrices with the same dimensions and produces a matrix.[13] The interaction between sensors and physical scenarios can be represented mathematically as the Hadamard product operation between the original input matrix and the operator matrix, as defined in Equation (3)

$$Y_{mn} = X_{mn} \odot f_{mn} \tag{3}$$

The structured output matrix Y_{mn} is obtained by mapping the original input matrix X_{mn} through the operator matrix f_{mn} within sensors. By adjusting operator characteristics through the coordinated design of materials and devices, sensors can transform unstructured information into diverse features. Light serves as a high dimensional information carrier. In vision structuring, the input matrix that accurately represents the light field contains multidimensional light information, denoted as $X(x, y, z, p, t, \lambda, \psi, \varphi, \theta, \Phi)$,[14] where (x, y, z) defines position, (p, t) represents spatiotemporal information including intensity and time, (λ, ψ, φ) denotes the spectrum, polarization, and phase, respectively, and (θ, φ) signifies the angle of light light propagation. The operators within vision sensors describe the responsivity to various light dimensions. Thus, by utilizing Hadamard product operation, vison sensors enable transforming raw visual data into multidimensional structured vision (Figure 1b,ii) such as edge, motion, color, depth, etc.

In-sensor computing integrates perception, memory, and processing functions within sensors, which enables sensory terminals to extract essential information and achieve data compression and structuring. Processing information directly in sensory terminals reduces the data volume transferred to subsequent processing units, thus reducing time latency and power consumption. In this review, we adopt the most data-intensive application—vision sensors—as an example for the demonstration of the in-sensor computing. We systematically discuss the visual processing functionalities with electronic, optical, and optoelectronic devices. Particularly, we explore the hardware implementation of optoelectronic devices for in-sensor visual processing, which can compress and structure multidimensional vision without extra optoelectronic conversion. More specifically, we explore the resistive switching mechanisms of optoelectronic

devices, classifying them into nonvolatile and volatile devices. Finally, we provide a perspective on optoelectronic devices for in-sensor computing including potential challenges and application scenarios.

2. Computational Hardware for Vision Compression and Structuring

The visual processing is primarily affected by three types of data redundancy: a) Encoding redundancy: using longer bit codes to represent grayscale values. b) Spatial and temporal redundancy: unnecessary repetition of spatial and temporal information in adjacent pixels. c) Irrelevant information: information unrelated to the intended use. Conventional CMOS image sensors can only collect the information from physical stimuli, requiring computation units and complex algorithms for visual processing (compression and structuring). Specifically, the encoder is required to create compressed representation of images, while the decoder can produce reconstructed output images. For vision structuring, analog signal processors (ASPs) and digital signal processors (DSPs) can implement diverse machine-learning algorithms to extract features across multiple dimensions. However, the data traffic between sensors and computation units leads to power consumption and time latency, thus requiring the information processing functions in/near sensory terminals. In this section, we discuss the hardware implementation with electronic, optical, and optoelectronic devices for visual information compression and structuring near or within sensors.

2.1. Electronic Computing

Electronic computing refers to the manipulation and processing of information using electronic components, spanning from basic electronic building blocks to advanced architectures. It employs established silicon-based technologies and emerging electronic devices to perform computational tasks. For CMOS technology, the electronic computing hardware for visual processing mainly relies on the integration of ASP, analog-to-digital converters (ADCs) and DSP. ASPs are commonly custom-integrated circuits (ASICs) with function-specific circuits designed for specific image processing tasks, such as amplification, filtering, etc. Through circuit and function optimization, combined with efficient power management, ASP hardware can achieve low-power image processing.[15] DSP consists of memories, arithmetic logic units (ALUs), and control units. The ALU can perform both Boolean and arithmetic operations to build processing cores. The multiply-accumulate (MAC) operation is the most critical for feature extraction and effective compression encoding. However, computation with logic gates are inefficient and consume lots of resources despite their universality and robustness. Improving computational parallelism through the integration of multiple cores (e.g., GPU) at the hardware level requires substantial computational resources. With advancements in data-centric computing, data transmission between electronic hardware units have dominant overall latency and energy consumption.

Computing in memory (CIM) refers to a computing architecture that can perform in situ data computations within memories. By interfacing directly with analog signals from photosensors, the memories enable the in-memory computing for visual processing, thus eliminating bandwidth limitations and reducing data movement. The memory array is organized as a random access architecture. The storage units are placed at each intersection location of word lines and bit lines for data storage (**Figure 2a**). Figure 2b shows the electronic memories for CIM, classified as volatile memories (VMs) and nonvolatile memories (NVMs).[16] Volatile dynamic random access memory (DRAM) uses charges in the capacitor for information storage and requires periodic refreshing to retain information.[17] Volatile static RAM (SRAM) stores data based on bistable circuits.[18] NVMs, such as Flash, FeFET, and resistive memories, employ different mechanisms—floating gate modulation, ferroelectric switching, resistance changes—for data storage. Electronic memories are based on physical principles like Kirchhoff's law and charge distribution for analog computing, thereby realizing computation such as logic gates and MAC operations for visual processing. However, electronic memories still require coupling with other sensory systems for near-sensor computing. Consequently, the data transmission between sensors and processing units leads to extra time delay and power consumption. Direct integration of visual processing into each pixel of vision sensor offers a potential strategy to overcome these challenges.

2.2. Optical Computing

Optical computing, taking advantages of the tunable transmission characteristics of waveguide-integrated optical devices induced by the variable refractive index, performs computing in the optical domain.[19] Photonic integrated circuits compactly integrate optical waveguides, modulators, filters, and detectors,[20,21] on a single chip. Image sensing, image processing, and recognition can be realized by computational tasks with the assist of the on-chip optical matrix arrays and optical sensor arrays.[22–24] Figure 2 shows three typical reconfigurable integrated photonic elements, including Mach–Zehnder interferometer (MZI), microring resonator, and tunable splitter. The strategies for tunable optical transmission in on-chip optical devices primarily include electro-optic effect, thermo-optic effect, and all-optic effect.[25] The Pockels effect and the plasma dispersion effect are two typical electro-optic response, allowing to modulate optical phase and intensity via refractive index changes under an external electric field. Simultaneously, refractive index is sensitive to temperature variation. Therefore, microheaters are typically utilized to control optical phase in on-chip devices due to the thermo-optic effect. However, the dynamic response is generally lager than MHz, limited by slow thermal diffusion. Moreover, optical transmission in dielectric waveguides can be controlled by another optical beam, mainly resulting from saturable absorption and optical Kerr effect. Recently, optical phase change materials have drawn much attention for tuning optical phase and intensity with nonvolatile performance, thereby bringing about the near-zero-power-consumption computing.[26] Nowadays, nonvolatile optical devices with large scale for optical matrix are usually achieved by integrating phase change material with microheaters, such as TiN_x and Si p-i-n junction onto optical waveguide.[27–29]

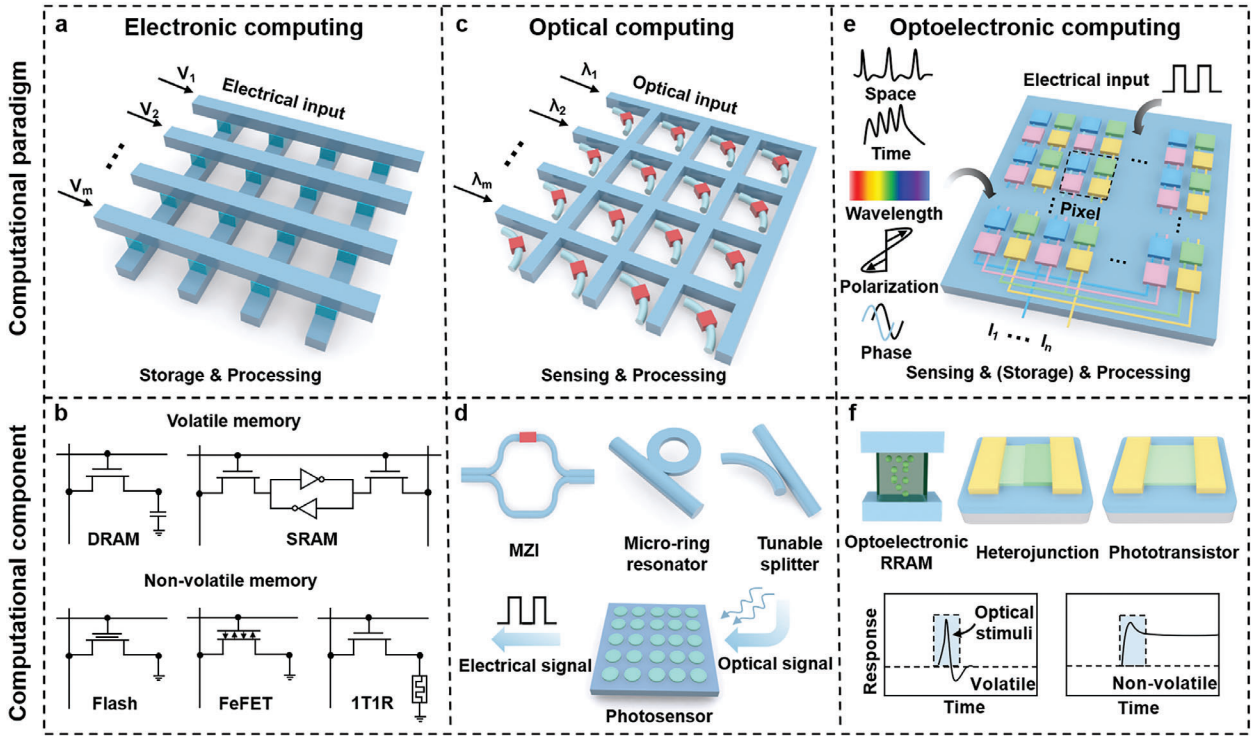

Figure 2. Computational hardware for visual processing. a) Electronic computing based on electronic device array. b) Electronic devices for CIM, including VMs (DRAM, SRAM), and NVMs (Flash, FeFET, and resistive memories). c) Optical computing based on optical devices. d) Structure of typical reconfigurable integrated photonic elements: MZI, microring resonators and tunable splitter. Optical signals are then converted through on-chip/off-chip optoelectronic interconnection. e) Optoelectronic computing based on multidimensional optoelectronic devices. f) Optoelectronic devices with volatile/nonvolatile characteristics for optoelectronic computing.

Comparing with electronic computing, optical computing offers higher bandwidth, parallelism, lower energy consumption (Figure 2c), benefitting from fast dynamic response of optical devices, wavelength division multiplexing in photonic system, and small optical loss in dielectric waveguide. Optical multiplexing technologies, including wavelength division multiplexing (WDM), mode division multiplexing (MDM), and polarization division multiplexing (PDM), significantly enhance the transmission efficiency. WDM operates by transmitting signals at different wavelengths,[30] MDM utilizes various transmission modes within optical waveguide,[31] and PDM employs two orthogonal polarization states for information transmission.[32] These multiplexing methods can be used independently or in combination to optimize data transmission density and reduce signal interference. However, optical devices typically range in size from micrometers to millimeters. Thus, they demonstrate lower integration levels compared to electronic counterparts, as electronic devices can be extremely small (<2 nm).[33] Additionally, the benefits of optical computing are compromised by optoelectronic conversion, resulting in extra transmission losses, delays, and energy consumption.

2.3. Optoelectronic Computing

Optoelectronic computing integrates perception, memory, and computation to directly compress and structure multidimensional optical information. By designing the light–matter interaction, the photoresponsivity can be modulated within both optical and electronic domains (Figure 2e). Visual information mapped onto the optoelectronic array can be directly converted into compressed or structured features.

Multidimensional visual processing requires the coordinated design of the materials and structures within the optoelectronic devices. Optoelectronic devices with volatile and nonvolatile characteristics realize temporary data storage via photo-induced resistive switching materials (Figure 2f). By using space and time dependent plasticity, optoelectronic devices enable direct processing of raw vision across both temporal and spatial dimensions. In space dimension, heterojunctions can produce reconfigurable positive/negative photoresponsivity through band structure engineering[34] and electrical modulation.[35,36] The reconfigurable response can construct convolution kernels with different functions to implement convolutional operations, such as edge extraction, sharpening, blurring, etc. Moreover, light-induced electrochemical reactions[37] can establish a superlinear relationship between input intensity and output amplitude, enabling feature enhancement.[38] In time dimension, volatile devices exhibit temporal evolution and summation of conductance.[39,40] They can integrate information from both current and previous visual inputs, enabling the effective processing of dynamic visual scenes. The dynamics of photogenerated carriers and charge trap centers manifest as photocurrent relaxation in phototransistors, regarding as a short-term

Table 1. The characteristics of optoelectronic devices for visual processing in different dimensions.

Dimensions	Processing function	Characteristics of optoelectronic devices	Refs.
Intensity	Convolutional operations	Reconfigurable positive/negative photoresponsivity	[34–36]
	Feature enhancement	Superlinear relationship between input intensity and output amplitude	[37, 38]
Temporality	Motion extraction	Temporal evolution and summation	[39, 40]
		Reconfigurable photoresponsivity for difference operations	[36]
	Event-based sampling	Integration of photodetectors with capacitors and resistors	[41, 42]
Wavelength	Color extraction	Narrowband materials for wavelength-selective bandpass filters	[50–54]
		Broadband materials for multispectral perception	[34, 55, 56]
Polarization	Information extraction in extreme environments	Metalenses with chiral plasmonic nanoparticles	[58–60]
		Integration of low-symmetry materials	[61–63]
Phase	Planar phase holography	Metalenses with predefined phase profiles as phase modulators	[64, 65]

memory characteristic that can be leveraged for processing temporal information. Nonvolatile devices with tunable and reconfigurable response also enable motion perception by interframe difference calculations.[36] Additionally, integrating photodetectors with capacitors and resistors can create event-driven motion sampling[41,42] with embedded dynamic vision sensor capabilities.[43–46] In spectral dimension, materials with varying transmission coefficients can serve as wavelength-selective bandpass filters extract color features.[47–49] Utilizing the narrowband response characteristics of emerging materials, such as quantum dots[50–54] enables the feature extraction at specific wavelengths. The broadband response can enhance the recognition accuracy for multispectral imaging.[34,55,56] Van der Waals MoS_2/WSe_2 heterojunctions with gate-tunable optical response can also realize compact and high-performance computational spectrometers. In polarization dimension, polarization information can be structured in extreme environments (e.g., fog, underwater) through the interaction of visual input with polarization-sensitive photosensors.[57] The highly anisotropic materials and metasurfaces have advanced in polarization-sensitive photosensors for detection of linear/circular polarization and reconstruction of full Stokes parameters. The anisotropic materials can induce a polarization-selective photoresponse owing to their intrinsic dichroism effect.[58–60] Metasurfaces designed with chiral plasmonic nanoparticles exhibit selective sensitivity to different polarization states.[61–63] In phase dimension, metasurfaces can locally modify the phase in reflection or transmission by geometric design. Metasurfaces with a predefined phase profile can serve as a phase modulator to extract specific phase information, which is particularly suitable for implementing planar phase holography.[64,65] The characteristics of optoelectronic devices for visual processing across different light dimensions are summarized in **Table 1**.

Compared to electronic and optical computing hardware, optoelectronic devices perform optoelectronic conversion and processing simultaneously, eliminating the need for data transmission between optical and electronic components. The operation speed is only limited by the optoelectronic conversion of individual devices. Therefore, with the proper design of materials and device structure, ultrafast vision compression and structuring can be achieved.

3. Optoelectronic Nonvolatile Switching Devices

Optoelectronic nonvolatile devices can exhibit conductance changes under external light stimulation. In the context of in-sensor computing, the nonvolatile response of these optoelectronic devices can be modeled as operators for in situ processing of the raw data. The light-dosage-dependent nonvolatile characteristics of optoelectronic devices can also be utilized to locally store the main features of sensory information. The in situ processing/storage capability of optoelectronic nonvolatile devices greatly mitigates communication bottlenecks between components in intelligent vision systems. In this section, we will overview the nonvolatile switching mechanisms of optoelectronic devices, including charge-assisted direct photon-carrier conversion, photomodulated metallization/vacancy migration, photochemical reaction, photo-phase transition, photoferroelectric switching, and photomagnetization.

3.1. Charge-Assisted Direct Photon-Carrier Conversion

Direct photon-carrier conversion refers to the process, in which photons are directly converted into charge carriers (**Figure 3a**). PN junctions or heterojunctions can effectively generate photovoltage and photocurrent without external bias through the photovoltaic effect. In monolayer WSe_2, a programmable photodiode can be created using split-gate electrodes through electronic modulation with different polarities.[66] Image sensors can form artificial neural networks (ANN) through physical parallel connections of subpixels, with continuously tunable weights by electronic modulation. ANN vision sensors can adapt both supervised and unsupervised learning algorithms for ultrafast image recognition and encoding.[67] However, constant gate voltages need to be applied to maintain the photoresponsivity, which inevitably leads to additional energy consumption. Thus, the floating gate (FG) can be adopted to modulating conductance switching with nonvolatile states and long-term retention. Electronic stimuli serve as the programming source for conductance switching in computing tasks. The WSe_2 photodiode with $Al_2O_3/HfO_2/Al_2O_3$ floating gate achieves nonvolatile electrical programming, allowing operation under zero bias without continuous electronic modulation. The 2D2R1C pixel with WSe_2 photodiodes can form event-driven vision sensors,[42,43] which

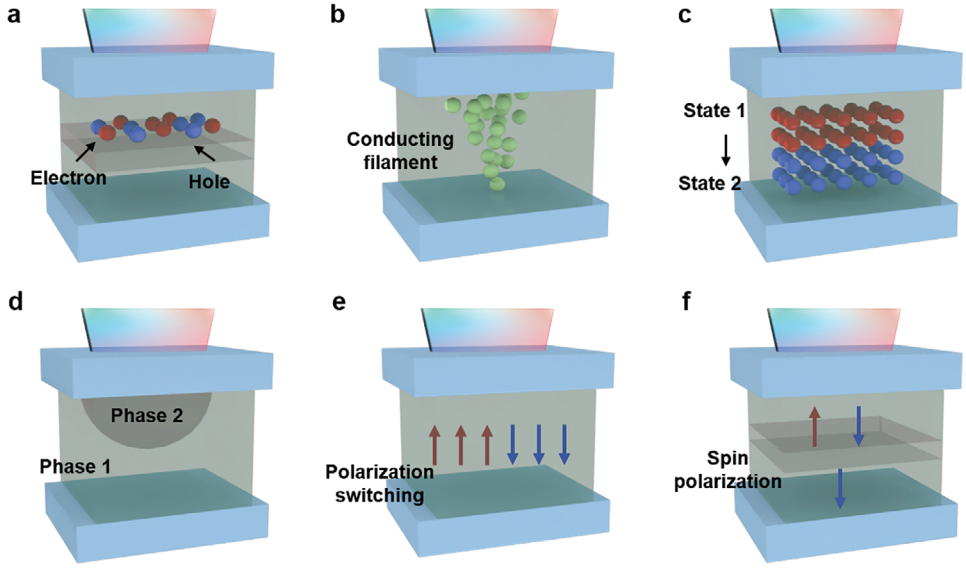

Figure 3. The switching mechanisms of optoelectronic nonvolatile devices. a) Charge-assisted direct photon-carrier conversion. Photons are directly converted into electron-hole pairs. b) Photomodulated metallization/vacancy migration. Light modulates metal ions/vacancy redistribution between electrodes. c) Photochemical reaction. Light induces a chemical reaction in the functional layer to regulate the conductive level of the devices. d) Photo-phase transition. The external light induces structural phase transitions. e) Photo-ferroelectric switching. Light induces ferroelectric polarization. f) Photomagnetization. Light induces spin polarization in a magnetic free layer.

only react to light intensity changes in the visual scene and greatly reduce the redundant data. The temporal differentiation of light intensity allows sensors to capture changes in intensity based on events. Event-driven vision sensors encode motion into sparse spikes with tunable amplitudes and polarities, enabling construction of spiking neural networks (SNNs) for motion recognition tasks. The FG layer can also utilize photosensitive materials to achieve conductance switching. The BP/Al_2O_3/WSe_2/h-BN heterostructure employs electronic programming to modulate the tunneling and thermal excitation process of photogenerated carriers from WSe_2 to h-BN.[36] The heterostructure exhibits both nonvolatile positive and negative photoconductive properties. Thus, reconfigurable photoconductive states enable the establishment of convolutional kernels for edge detection. Motion perception and recognition can also be achieved through inter-frame difference calculation. Moreover, the charge carriers stored at the interface can be precisely modulated by electronic and light stimuli. In WSe_2/h-BN heterostructure, photoexcited holes in WSe_2 are transmitted through h-BN and captured at the interface between h-BN and Al_2O_3 with back gate modulation. The captured holes serve as effective local gates for nonvolatile programming. With continuous light stimuli, the charge on the interface gradually recombines to achieving photo-erasure. The WSe_2/h-BN heterostructure can encode the spatiotemporal information, thereby perceiving multiple information related to targeted motion modes.[68]

3.2. Photomodulated Metallization/Vacancy Migration

Resistive switching materials are promising for future high-density, low-power, low-latency memory systems.[69,70] In conventional electronics, an external electric field can induce the formation of metal conducting filaments[71] or the migration of oxygen vacancies,[72] enabling nonvolatile resistive switching behavior. The optoelectronic nonvolatile memory can be realized by photomodulated metal filament dynamics/vacancy redistribution (Figure 3b).

Redox reactions and ion migration are essential steps in the metal filament formation/rupture process. The external light field induces photogenerated carriers in switching medium, which in turn modulates the key steps described above. Light stimulus can be used to modulate the oxidation process of metal filaments. A resistive random access memory (RRAM) with sandwich-like Ag/switching medium ($MoSe_2$/Bi_2Se_3 nanosheets in PMMA)/ITO structure featured a near-infrared (NIR) light-assisted reset behavior.[73] The resistive switching behavior of the device originated from the Ag conducting filaments. The $MoSe_2$/Bi_2Se_3 heterostructure facilitated the separation of photogenerated electrons–hole pairs, inducing an internal electric field. Under this internal electric field, the holes struck the Ag filaments and promoted the oxidation reaction of Ag. As a result, the NIR light induced the rupture of the conducting filaments. Photogenerated carriers can also affect the speed of ion migration. For example, optoelectronic RRAM with an ITO/ZnO/Ag structure can exhibit nonvolatile resistive switching behavior in response to optical and electrical stimuli.[74] Under illumination, the photogenerated electrons can draw the Ag^+ toward the switching medium, leading to the formation of a conductive filament. This process facilitated the transition of resistance state from a high resistance state (HRS) to a low resistance state (LRS). Therefore, the external light field can accelerate the speed of ion migration in the switching medium. In summary, the photogenerated carriers give the two-terminal RRAM devices a nonvolatile photoresponse by affecting the redox reaction rate and the ion migration speed. This photoresponse can be used to store the light

field intensity. Moreover, photomodulated artificial synapses can be realized by utilizing the above photoresponse.

Localized light–matter interactions can be used to induce vacancy redistribution. When irradiated with light, the photogenerated carriers create an inhomogeneous distribution within the bulk material. At the surface of the material, the enriched photogenerated electrons are easily trapped by the defects, creating an internal electric field. This light-induced internal electric field affects the ion migration inside the material, leading to the redistribution of vacancies.[75] For example, an external light stimulus can induce the annihilation of vacancies in $CH_3NH_3PbI_3$ ($MAPbI_3$). As a typical perovskite material, $MAPbI_3$ has a high optical absorption coefficient.[76] The resistive switching behavior of $MAPbI_3$-based memory mainly depends on the formation and annihilation of iodine vacancies.[77] Under illumination, the iodine vacancies in $MAPbI_3$ are unstable, and they spontaneously spread and combine with iodine interstitial ions. Therefore, light will promote the annihilation of iodine vacancies. Light can also facilitate the migration of vacancies. In optoelectronic RRAM with a device structure of ITO/PMMA/$CsPbBr_3$ quantum dots (QDs)/PMMA/Ag, both Ag metal filaments and bromide vacancy filaments induced the resistive switching.[78] Under light, photogenerated electron/hole pairs were separated and trapped. The trapped carriers created an additional internal electric field that enhanced the migration of bromide ions toward the anode. Therefore, the inhomogeneous photogenerated carriers and trap-induced space charge separation both contribute to the generation of an internal electric field, leading to the redistribution of bromide vacancies.

For RRAM that relies on metal filament/vacancy migration, redox reaction, and ion/vacancy migration are closely related to the distribution of electric potential and chemical potential. The external light field induces inhomogeneous generation/distribution of carriers in the switching medium, which significantly affects the electric field and energy distribution. As a result, the electric and chemical potentials in the device change in response to light stimulus, endowing the RRAM with a nonvolatile photoresponse.

3.3. Photochemical Reaction

The photochemical reaction usually refers to the chemical reaction of substances due to light irradiation (Figure 3c). In the context of highly scaled modern electronics, solid-state photochemical reactions (e.g., diarylethene undergoing a transition between an open-ring state and a closed-ring state under the light of different wavelengths[79]) are preferred to avoid the complex fabrication process of building a miniaturized environment for liquid-state reactions. The photochemical reactions enable the modulation of device conductance mainly by the formation of highly conductive material and the interaction between photochromic molecules with adjacent material, respectively.

Highly conductive materials can be formed by photochemical reactions. A two-terminal optoelectronic resistive random access memory (ORRAM) with a structure of Pd/MoO_x/ITO exhibits nonvolatile resistive switching and light-tunable synaptic behaviors.[37] When the ORRAM is exposed to ultraviolet (UV) light, the photogenerated electrons induce the transformation of Mo^{6+} into Mo^{5+}. The photogenerated holes react with the water molecules absorbed in MoO_x film to generate protons (H^+), which in turn form highly conductive H_yMoO_x. The device conductance increases because of the formation of metallic H_yMoO_x. The exhibited light-dosage-dependent memory effect of ORRAM devices enables the visual pre-processing function to enhance the image contrast.

Photochromism describes the phenomenon of photo-induced transitions of a molecule between isomers with different absorption spectra.[80] The properties of photochromic molecules change during photoisomerization, affecting the interaction with adjacent materials. For example, photochromic molecules at the interface can modify the interfacial barrier under light stimulus.[81] The light stimulus induces a transition between trans- and cis-isomer of photochromic azobenzene (Azo) at the MoS_2/Azo/Au interface, modulating the tunneling thickness at the interface. In addition, the photoisomerization of Azo affects the level of Fermi energy levels in MoS_2. The isomerization of Azo affects the carrier transport, realizing a multibit nonvolatile memory. Differences in the electronic structure of the isomers can be used to design photo-controlled carrier trapping behavior. For example, a blend of a photochromic diarylethene moiety (DAE-Me) with a semiconducting polymer (poly(3-hexylthiophene), P3HT) provided a nonvolatile photoresponse.[82] The open and closed isomers of DAE-Me have different energy level matching sceneries with P3HT. Therefore, different trapping behaviors can be achieved in the blend by light-induced isomer transition.

In optoelectronic devices, carriers transport through the active region (switching medium in a two-terminal device as well as the channel in a three-terminal device) and the active region/electrode interface. For a two-terminal device, the photochemical reaction forms highly conductive material in the active region. This highly conductive material forms a percolating conductive network between the electrodes, which changes the conductance of devices. For a three-terminal device, incorporating photochromic molecules into the channel material enables a photomodulated carrier trapping process. In addition, the active region/electrode interface can be modified with photochromic molecules. Such interfacial modifications can induce light-controlled interfacial barrier shape which affects the current through the interface. Based on the above mechanisms,[83,84] optoelectronic devices demonstrate light-dose or wavelength-dependent nonvolatile response, which realizes optically controlled multilevel memory and optoelectronic neuromorphic device.

3.4. Photo-phase Transition

The variations in external temperature, electric field, optical field, and doping can induce insulator-to-metal transition,[85,86] semiconducting-to-metallic phase transition,[87,88] and transition between crystalline/amorphous phases.[89] The injection of external charge induced changes in electronic structure, destabilizing the phase of the material.[88] Light stimulation with high-energy photons can also induce strain in the lattice. These mechanisms facilitate the light-induced phase transition. The phase transitions induced by an external light field (Figure 3d) have paved

the way for advancements in optoelectronic nonvolatile memory and neuromorphic device technologies.

Light irradiation with high photon energy induced defects in the lattice, leading to the generation of strain. The strain decreased the lattice stability, promoting the occurrence of structural phase transition. Vanadium dioxide (VO_2) exhibited ultraviolet (UV)-induced nonvolatile phase transition.[90] This phototriggered phase transition can be reversibly modulated by electrolyte gating. The photon energy of UV light is larger than the energy which is required to remove one oxygen atom at the surface of VO_2 film. Therefore, UV light irradiation can induce oxygen vacancies. The oxygen vacancies can further promote electronic phase transition, inducing strain in VO_2.[91] This strain facilitated the phase transition of VO_2 from a low-symmetry monoclinic phase to a metallic phase. The realized VO_2 optoelectronic memory has a good multilevel retention characteristic (>4000 s). The resistance of VO_2 devices can serve as the synaptic weights to build an artificial neural network, or the convolution kernels to perform the edge enhancement. By utilizing the nonvolatile memory of the device, motion detection can also be achieved by using different device arrays to sense images at different frames.

Photo-induced carrier leaps to high energy levels reduced phase stability, facilitating the structural phase transition. For example, the oxygen-doped MoS_2 (O-doped MoS_2) exhibited a light-induced phase transition.[92] Upon electrical stimulation, oxygen vacancies were induced in O-doped MoS_2, injecting electrons into the MoS_2. The injected electrons destabilized the lattice of 2H-MoS_2, transforming the 2H phase into the 1T phase. When exposed to light, the electrons in MoS_2 leaped to higher energy levels, decreasing the stability of the 1T-MoS_2 lattice. Therefore, the O-doped MoS_2 changed to the 2H phase. With the assistance of light-induced unidirectional and reversible (under electrical stimuli) resistive switching behavior, the O-doped MoS_2-based device demonstrated reproducible switching performance up to 200 cycles of alternating electrical and optical pulses. Taking advantage of light-intensity-dependent retention properties, the device can be used for image pre-processing, reducing the noise of the image.

Furthermore, an external light field can introduce variations in temperature within materials to induce a nonvolatile phase transition. Specifically, by changing the temperature of the $Ge_2Sb_2Te_5$ (GST), the GST can undergo a transition between an amorphous phase and a crystalline phase. The light stimuli drive the temperature change in the GST, which in turn induces a phase transition.[89] The external light field can be applied through a waveguide[93] or free space[94] to modulate GST-based optoelectronic devices. Furthermore, by introducing a waveguide-integrated plasmonic nanogap in the device, the light–matter interaction can be enhanced, and optical nonvolatile switching can be realized at lower switching energy.[93]

In optoelectronic nonvolatile devices, phase-change materials are often used as channels for carrier transport. In this way, the carrier transport behavior is modulated by changing the phase of the material. The phase transition involves a change in energy. Sufficient energy from the environment is required to overcome the phase transition energy barrier. An external light field can be used as a source of energy to induce the phase transition in the material. After the disappearance of the external light stimulus, maintaining the stability of the new phase is essential for optoelectronic nonvolatile devices. Light sources with high photon energy can induce microscopic lattice structure variations, promoting stable phase transition by the creation of strain in the lattice. Alternatively, doping can induce the phase which is normally unstable under ambient condition. Afterward, the light stimulus can drive the crystal to transform into a thermodynamically stable phase, achieving a nonvolatile photoresponse.

3.5. Photoferroelectric Switching

Ferroelectric materials with spontaneous polarization are promising candidates for nonvolatile devices. The polarization can be switched by the electric field and maintained stable. The light stimuli can also change the energy landscape of ferroelectric materials and induce polarization switching, which makes ferroelectric devices potential for visual processing (**Figure** 3e).

There are two types of photoferroelectric switching, which are based on the photovoltaic effect and imprint field, respectively. The photovoltaic effect is based on the noncentrosymmetric crystal structure of ferroelectric materials.[95–99] The light stimuli will generate nonequilibrium carriers, which spontaneously move toward one direction and produce a constant current. The current direction is determined by the relationship between the light polarization direction and crystal structure. This photovoltaic current can create an electric field across the ferroelectric materials. To create an electric field larger than the coercive field of ferroelectric materials, the illuminated area should be separated from the switching area.[99] In addition, the contact area should be reduced to enhance the current density. The magnitude of the electric field can be modulated by the light intensity, light polarization direction, and contact area. Based on this mechanism, the ferroelectric polarization can be reversibly switched by light stimuli. Under different polarization states, the ferroelectric devices exhibit different electronic properties, such as resistance. Therefore, the visual information (intensity and polarization) can be stored in the ferroelectric devices.

The imprint field of ferroelectric materials is induced by the asymmetric interface conditions, which can be imposed by the growth process or different contacting electrodes.[100–104] The imprint field functions as the built-in electric field to switch the polarization. Without an external electric field, the energy landscape of ferroelectric materials is asymmetric, making one polarization state more energy-favorable. When the ferroelectric material is switched to the unfavored polarization state by an electric field, the energy barrier to switch back to the favored polarization state is lower, due to the facilitation of the imprint field. The light stimuli can provide the energy to overcome the energy barrier. Ferroelectric semiconductors like α-In_2Se_3 with small bandgap can directly respond to light stimuli in entire visible spectrum, which is appropriate for visual information processing.[105,106] The photogenerated carriers can compensate for the screening charges induced by ferroelectric polarization charges, which reduce the screening electric field. Therefore, the imprint field exceeds the screening electric field and cause polarization relaxation. For ferroelectric materials with large bandgap, the optically controlled ferroelectric devices are consisted of ferroelectric/semiconductor heterostructures, in which the semiconductor is photoactive. The photogenerated carriers in semiconductor compensate for the

screening charges near the ferroelectric interface and induce ferroelectric switching.

Based on the above mechanism, various optoelectronic devices have exhibited optical control of device conductance and nonvolatile memory. The device conductance shows a strong dependence on the light intensity and exposure time, which allows multilevel memory suitable for dense storage and neuromorphic computing. In addition, some optoelectronic devices exhibit short-term memory under low-dosage light illumination and long-term memory under high-dosage light illumination, which allows the emulation of forgetting and memory process.

3.6. Photomagnetization

Photomagnetization involves using light to induce changes in the magnetic properties of materials, which includes changes in the ordering temperature, magnetization, remanent magnetization, and coercive field after the light illumination (Figure 3f). The optical control of magnetism mechanisms typically relies on magneto-optical (MO) effects and photogenerated carriers, light-induced magnetic phase transitions, light-induced heating, spin photovoltaic effects (SPVE), and bulk photovoltaic effects (BPVE).[107,108] Photomagnetization provides great potential in advancing rapid magnetic storage and spintronics, owing to its high speed, noncontact, and flexibility. A major focus of current research is in all-optical switching (AOS) of magnetism to achieve faster and more energy-efficient memory device.[108]

All-optical switching (AOS) with laser pulses has been achieved in a wider spectrum of materials. These include various alloys,[109] multilayers,[110] and even RE-free Co-Ir-based synthetic ferrimagnets (SFIs).[111] Laser-induced heating near the Curie temperature is intricately linked to the switching mechanisms.[107] The incident laser can facilitate the transfer of heat, allowing the temperature to reach a level where the required exchange of angular momentum becomes minimal. Subsequently, the transfer of angular momentum from the light to the sample becomes adequate to induce the desired magnetization switching. Through integrating this kind of optically switchable Gd (Fe,Co) film into an MTJ device, an all-optical switching of a magnetic tunnel junctions (MTJ) is achieved. The switching is read out electrically through measuring the tunneling magneto[105,106]resistance (TMR).[112] All-optical magnetization switching has also been achieved in the atomically 2D ferromagnetic semiconductor, CrI_3. Spin angular momentum transfer from photoexcited carriers to local magnetic moments underlies the switching process.[113]

The optical manipulation of magnetism typically relies on ferromagnetic or antiferromagnetic materials. However, there is a potential for photo-induced magnetism in nonmagnetic materials, such as semiconductors and nanoparticles. This opens up new avenues for controlling magnetism using light, which could lead to more efficient and tunable magnetic devices. Light-induced ferromagnetism has been observed in WS_2/WSe_2 moiré superlattices, attributed to the enhanced spin–spin exchange interaction between moiré-trapped carriers and thus triggers the emergence of ferromagnetic order.[114] The inverse Faraday effect has led to the discovery of optically induced magnetization in plasmonic gold nanoparticles.[115]

4. Optoelectronic Volatile Switching Devices

Optoelectronic volatile devices can produce time-dependent conductance changes under optoelectronic stimuli. The volatile states contain spatiotemporal information, enabling time-sensitive visual processing. In the human retina, neurons with diverse functionalities are intricately connected, playing essential roles in sensing, fusion, and processing external stimuli. Optogenetics enables precise optical control over neuronal activity, contributing to the modulation of signal transmission in neurons. Volatile optoelectronic devices simulate the changes in membrane potential of biological neurons over time, contributing to the advancement of optoelectronic computing through optogenetics simulation. In this section, we will overview the mechanisms of optoelectronic volatile devices and their hardware implementation in simulating artificial optoelectronic afferent neurons, including optoelectronic Leaky Integrate-and-Fire (LIF) neurons, graded neurons, optical nociceptors, and multimodal neurons.

4.1. Optoelectronic LIF Neuron: Threshold Switching

The fundamental computation of LIF neurons involves the conversion of input signals into spike patterns (**Figure 4a**), which is widely applied in spike neural networks (SNNs). Spike-based processing results in sparse and efficient information transmission and compression. Conventional LIF model incorporates four key components: threshold-driven firing, "all-or-nothing" property, refractory period, frequency-dependent tunability (Figure 4b).[116] For optoelectronic LIF neurons, optical signals can be coupled into electronic spikes through optogenetic techniques. The firing frequency of LIF neurons can be modulated in different optical dimensions, thereby promoting the nervous ability to encode visual information.

The essential component of artificial optoelectronic LIF neurons is a threshold switching memory (TSM). As shown in Figure 4c, the TSM switches from HRS to LRS when the voltage exceeds the threshold (V_{th}). The TSM reverts to HRS when the voltage drops below the holding voltage (V_{hold}). The transition of threshold state results in the emission of a discharge spike. The integration of $Ag/Al_2O_3/Au$ threshold switch and photosensitive MoS_2 transistors simulates output spike characteristics under light modulation. The light-induced spikes are demonstrated via a resistance matching mediated by transistors and threshold switch. In addition, optoelectronic LIF neurons can be realized by charging and discharging circuits containing series combinations of capacitors, resistors, and an TSM. The charging circuit accumulates stimuli, transitioning the TSM from HRS to LRS. Subsequently, capacitor discharge triggers an output spike, and the neuron then enters a refractory period. Light-modulated TSM can emulate various characteristics of LIF neurons.

The core–shell InP/ZnS quantum dot-based LIF neuron demonstrates a light-induced transition from a nonvolatile resistive switching to a volatile threshold switching state.[117] Light modulation impacts intrinsic dynamics of LIF neuron dynamics and their synaptic connections. Light-induced weight modulation in optoelectronic synaptic devices affects the inputs of subsequent LIF neurons.[118] Furthermore, VO_2-based LIF

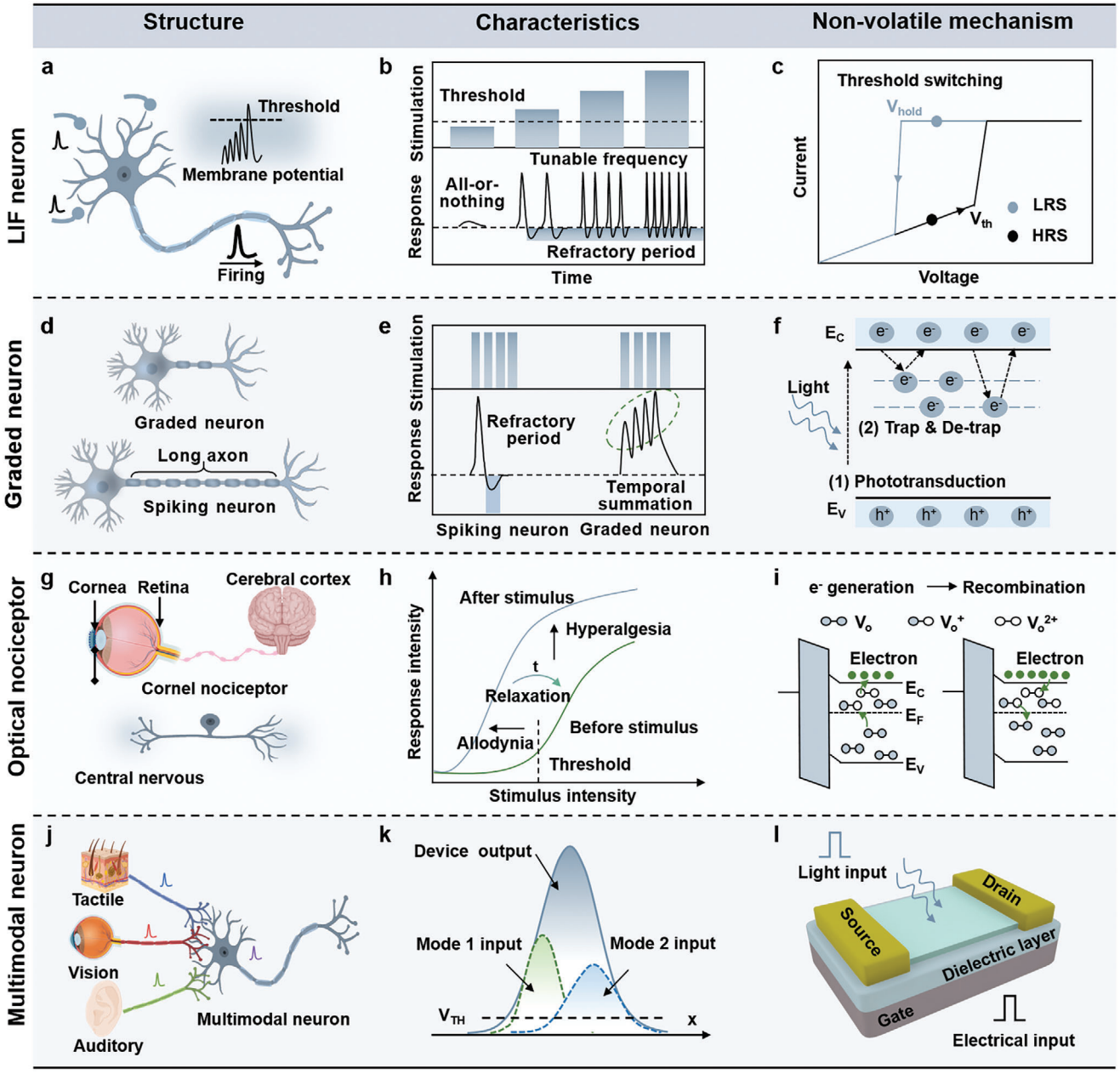

Figure 4. The characteristics and switching mechanisms of optoelectronic volatile devices. a) LIF neurons integrate preceding spikes, firing upon reaching threshold of membrane potential. b) LIF neurons shows four crucial features: i) threshold-driven firing: the neuron fires pulses once reaching a threshold; ii) "all-or-nothing" property: spike amplitude is independent of stimulus intensity; iii) refractory period: neurons become temporarily insensitive to stimuli after firing; iv) spiking frequency modulation: the firing rate depends on the amplitude and frequency of the stimulus. c) Typical *I–V* characteristic of volatile threshold-switching devices. d) The structure of graded neuron and spiking neuron, with graded neurons exhibiting shorter axons. e) Spiking neurons enter a refractory period under strong stimuli, while graded neurons respond to sequential stimuli through nonlinear temporal summation. f) The illustration of photogating effect, including phototransduction and charge trapping. g) The structure of the optical nociceptor under central nervous system modulation. h) The optical nociceptors show four crucial features: threshold, allodynia, hyperalgesia, and relaxation. i) The band diagrams for generation/recombination of electron at oxygen vacancies. j) Multimodal neurons integrate and process multiple sensory information. h) The schematic of multimodal integration. i) Optoelectronic comodulation of devices can achieve information fusion at the sensory terminals.

neurons, adapting to different resistance levels through multiple sensors, integrate cross-modal neuromorphic perceptual components. The artificial neurons enable encoding of illumination, temperature, pressure, and curvature signals into sparse sequences of spike.[119,120]

4.2. Graded Neurons: Photogating Effect

Graded neurons exhibit multilevel responses to continuous stimuli that mimic natural biological neuron behavior. Differing from spiking neurons, graded neurons can integrate signals over

time and space without the constraint of a refractory period (Figure 4d,e). The unique characteristic allows graded neurons to efficiently structure temporal information at sensory terminals through the spatiotemporal fusion.

Phototransistors based on the photogating effect provide a hardware platform for artificial graded neurons. Photogenerated carriers trapped in defect states can induce an electric field that act as gating terminals to increase/decrease the conductance of the photosensitive layer. The coupling of light stimuli and trap states results in volatile properties. The generated photocurrent will decay exponentially due to the release of carriers (Figure 4f). The current induced by continuous light input will be integrated in the time domain, as described in Equation (4)

$$I\ (t) = I_{\mathrm{dark}} + \sum \exp\left(-\frac{t}{t_0}\right) I_{\mathrm{o}} \tag{4}$$

where I_{dark} is the dark current, t is the time, t_0 is the time constant, I_{o} is the photocurrent. Therefore, the artificial graded neuron achieves temporal integration of different frames. Photogenerated holes trapped in the intrinsic shallow trapping states of MoS_2 to result in a relaxation decay in conductance and sublinear summation in the time domain. The process of trapping and release of carriers in trap states is affected by the gate voltage. The motion perception can effectively strike a balance between accuracy and efficiency with the appropriate temporal resolution. The processing of dynamic motion with different speeds can be achieved by modulating gate voltage to get various temporal resolution.[39] Moreover, trap states can be introduced into the materials or their interfaces through post-treatment.[121] The trap-state density in MoS_2 by post-treatment is comparable to the carrier concentration. The photosensitivity of the device under different illumination conditions can be dynamically modulated to realize visual adaptation.[122] Hydrophilic monolayers of MoS_2 can be synthesized by covalently introducing hydroxyl groups during the growth process. The replacement of some S atoms by hydroxyl groups in MoS_2 demonstrates strong charge trapping capabilities.[123] Furthermore, trap states can be introduced at the interface of the dielectric layer and MoS_2, demonstrating a voltage-tunable MoS_2 optical memory unit.

4.3. Optical Nociceptor: Redox Reaction of Oxygen Vacancies

Nociceptors are specialized peripheral sensory neurons that can not only function as alarm systems for threat detection but also process sensory information from various stimuli (Figure 4g). Optical nociceptors exhibit two crucial characteristics: allodynia and hyperalgesia.[124] Allodynia refers to a lowered threshold for heightened sensitivity to typically non-noxious stimuli, while hyperalgesia amplifies the response to noxious stimuli. Nociceptors can process visual stimuli using threshold properties and tunable sensitivity. For example, optical nociceptors are capable of extracting unique visual features, such as high intensity or specific wavelengths, to identify potential visual damage and filter out redundant visual information (Figure 4h).

The volatile light-induced threshold switching in optoelectronic devices stands as a pivotal characteristic for artificial optical nociceptors. In metal oxides, the light-induced generation and recombination of carriers at oxygen vacancies can dynamically modulate the carrier concentration (Figure 4i). Specifically, in amorphous indium gallium zinc oxide (a-IGZO), the ionization of oxygen vacancies induces a volatile positive photoconductance (PPC) effect.[125–127] Oxygen vacancies of a-IGZO exist in shallow donor states ($V_O{}^+$ and $V_O{}^{2+}$) as well as deep localized states (V_O) located ≈0.4–1 eV above the valence band edge (E_V). Under light stimuli, as depicted in Equation (5), the ionization of V_O generates excess electrons, thereby enhancing bulk conductance and simulating allodynia. Upon removal of noxious stimuli, optical nociceptors enter a relaxation phase, gradually restoring the threshold to preinjury level. The gradual neutralization of V_O simulates the relaxation process, as described in Equation (6)

$$V_{\mathrm{o}} \rightarrow V_{\mathrm{o}}^{+} + e^{-} \text{ and } V_{\mathrm{o}} \rightarrow V_{\mathrm{o}}^{2+} + 2e^{-} \tag{5}$$

$$V_{\mathrm{o}}^{+} + e^{-} \rightarrow V_{\mathrm{o}} \text{ and } V_{\mathrm{o}}^{2+} + 2e^{-} \rightarrow V_{\mathrm{o}} \tag{6}$$

During the relaxation phase, stimuli below the triggering threshold can reactivate nociceptors with heightened sensitivity. Cumulative stimuli can lead to increased retention of photogenerated electrons, thereby enhancing the photoresponsivity and simulating hyperalgesia. Electronic stimuli through the gate terminal can modulate the PPC effect, thus simulating pain regulation in the central nervous system by affecting electron generation/recombination. Furthermore, polarization in ferroelectric layers can modulate the photoresponsivity of artificial nociceptors.[128] By employing zirconium-doped hafnium oxide ($HfZrO_X$) as the ferroelectric layer, tunable optical nociceptors can be achieved in IGZO-based optoelectronic transistors. The depletion/accumulation of electrons at the $HfZrO_X$/IGZO interface due to polarization variations may hinder/enhance the recombination process, potentially prolonging/reducing relaxation time.

4.4. Multimodal Neuron: Fusion of Optoelectronic Stimuli

Multimodal neurons enable high-resolution integration of signals from various modalities, thereby improving decision-making and interaction with the dynamic world (Figure 4j). These neurons integrate multiple signals based on spatiotemporal principles, inverse principles, etc., to generate the responses for information compensation and multimodal correlation extraction (Figure 4k). The spatiotemporal principles describe that the integrated response is enhanced when the constituent unisensory stimuli are spatially congruent and temporally synchronous.[129] For artificial multimodal neurons, the nonlinear dynamic response depends on the temporal relationship of different modalities, conveying association information between multimodal stimuli.[130] The optical modulation of multimodal neurons represents a spatiotemporal signal integration method, allowing for local fusion and compression of visual information at the sensory terminals. Their volatile nature enables better adaptation to dynamic changes in multimodal environments.

Optoelectronic devices programmed through both light and electrical stimuli ideal for emulating artificial multimodal

Table 2. Benchmark of performance metrics for optoelectronic nonvolatile devices.

Nonvolatile mechanism	Perception range [dB]	Response time [ns]	Read voltage [V]	State number	Linearity	Retention [s]	Accuracy
Charge-assisted direct photon-carrier conversion	<140	~10^3	~0	>64	High	>10^3	≈100%
Photomodulated metallization/vacancy migration	/	<10^3	<0.1	>20	Low/ High	>10^4	<94.86%
Photochemical reaction	/	<10^1	<0.1	>256	/	>10^7	≈99%
Photo-phase transition	/	<10^3	<0.05	>20	High	>10^3	≈93%
Photoferroelectric switching	<43	<10^5	/	>150	High	>10^3	≈100%
Photomagnetization	/	~10^{-3}	/	2	/	/	/

neurons. Optical stimuli convey visual inputs to optoelectronic devices, while information from other modalities can be interconnected and converted to electronic inputs through various sensors (Figure 4l). The volatile optoelectronic devices enable multimodal computation for temporal-sensitive tasks. Volatile phototransistors can incorporate additional modalities into the gate terminal via a triboelectric nanogenerator or a separate pressure sensor.[131–135] The dynamic of charge trapping can be utilized to obtain relative timing information between visual and haptic stimuli. In_2Se_3-based optoelectronic devices offer promise as multimodal neurons due to the temporal dynamics from ferroelectric polarization switching.[136] The ferroelectric phototransistor enables reservoir computing for two modalities, with the timescales modulated by the gate voltage. Additionally, MoS_2 memtransistors and graphene chemitransistors can be integrated in a compact hardware platform to enhance efficient visuo-chemical information processing and decision-making.[137] The electronic outputs of optoelectronic devices also facilitate their flexible integration with other sensor components in basic logic circuits. Multimodal optoelectronic devices effectively integrate and compress light stimulation with pressure, audio, temperature stimulation, etc. However, it is crucial to match the normalized input intensities of the optical and electronic signals to ensure the correct integration and expected output weighting across different modalities.

5. Conclusions and Perspectives

Electronic computing, optical computing, and optoelectronic computing are three approaches to realize vision compression and vision structuring. Optoelectronic computing offers a highly integrated, ultrafast, and energy-efficient approach for visual processing, particularly beneficial for real-time and data-intensive applications. **Table 2** and **Figure 5** summarize the key metrics of nonvolatile/volatile optoelectronic devices for optoelectronic computing. For nonvolatile optoelectronic devices, various gate configurations provide multiple tunable states. PN junctions based on the photovoltaic effect can operate with zero power consumption. The abrupt current increase/saturation resulting from the formation of metal filament leads to lower linearity

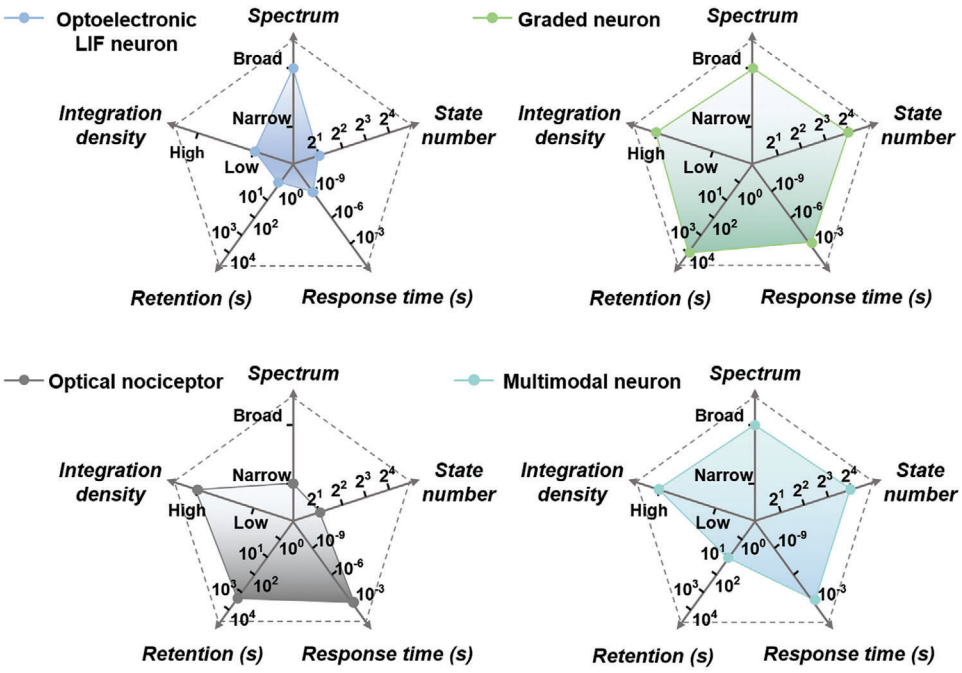

Figure 5. Benchmark of performance metrics for optoelectronic volatile devices. Radar charts compare the performance of optoelectronic LIF neurons, graded neurons, optical nociceptors, and multimodal neurons based on their integration density, retention, response time, state number, and spectrum.

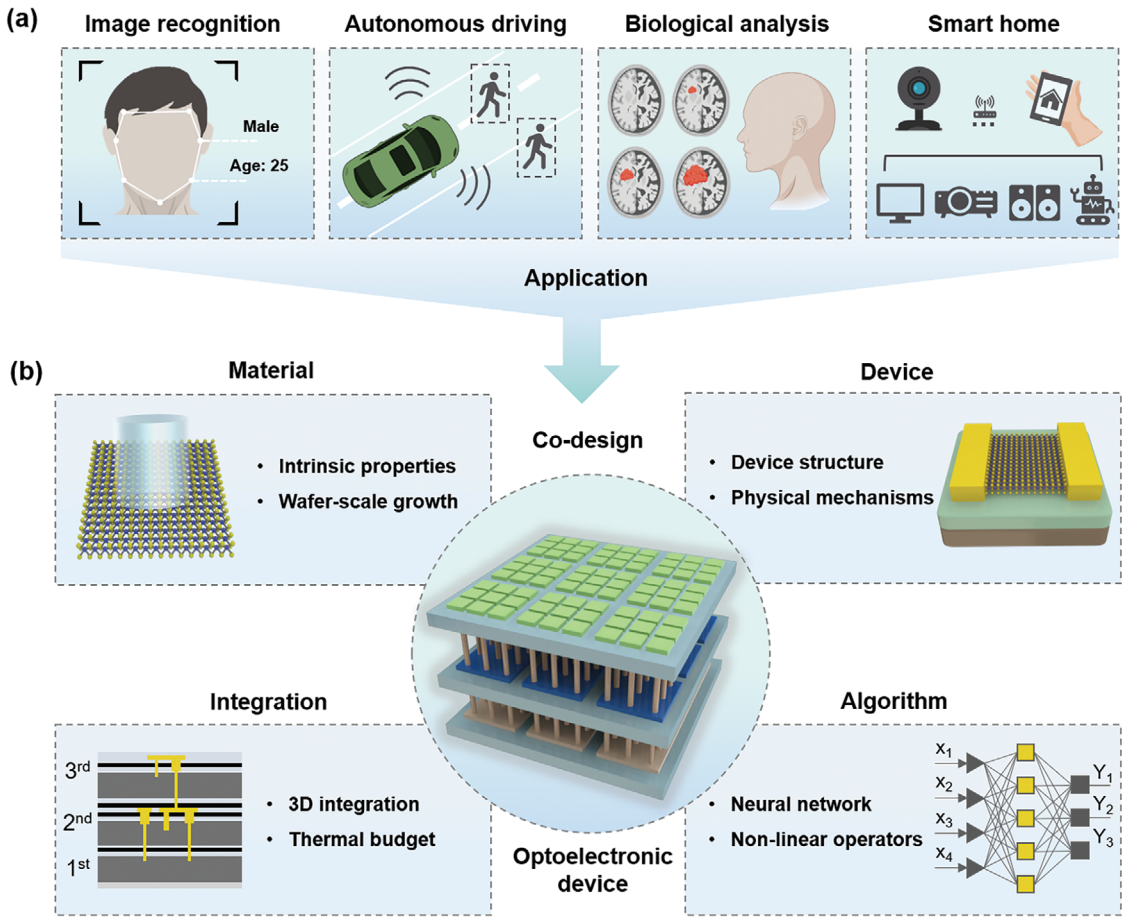

Figure 6. Codesign of optoelectronic devices. a) The potential applications of optoelectronic devices including image recognition, autonomous driving, biological analysis, and smart home. b) Codesign of optoelectronic devices from the aspects of material optimization, device design, integration technologies, and algorithms.

compared to oxygen vacancy migration. Nonvolatile photochemical reactions can achieve relatively stable switching states with long retention time. Photoferroelectric switching enables comprehensive optical control of ferroelectric polarization with low power consumption. The fundamental understanding of device physics in photomagnetization is still lacking, requiring further exploration in the realm of optoelectronic computing. For volatile optoelectronic devices, graded neurons, optical nociceptors, and multimodal neurons can be achieved at the single-device level with high integration density. The spatiotemporal summation characteristics of optoelectronic devices can obtain more computing states than threshold switching. Additionally, nonvolatile devices can realize longer relaxation time due to the redox reaction and trap dynamics, while exhibiting response time up to milliseconds.

The advancement of optoelectronic devices expands the scope of potential applications with customized features tailored to specific fields (**Figure** 6a). For instance, in image recognition, the high spatial resolution of optoelectronic devices enables accurate and detailed image analysis. In autonomous driving, ultrafast response, high dynamic range, and event-driven characteristics enables reliable operation under diverse environmental conditions to ensure safety and efficiency. For biological analysis, optoelectronic devices with high sensitivity facilitate early detection and precise identification of lesion sites. In smart homes, the focus on low power consumption and seamless integration with other smart devices promotes energy efficiency and user convenience. Furthermore, the evolution of optoelectronic devices is increasingly moving toward multidimensional vision sensing for sophisticated and intelligent perception across various industries. For example, integration of spectral and spatial information enables optoelectronic devices to extract environmental features across a broad spectrum. 3D sensing and imaging are advancing to provide precise depth perception, which is crucial for applications like autonomous driving and virtual reality. Based on the above potential applications and trends, the development of optoelectronic computing requires codevelopment and co-optimization of materials, devices, integration technologies and algorithms (Figure 6b).

5.1. Material Optimization

The prerequisites for large-scale optoelectronic computing including high-quality, wafer-scale growth of emerging materials and fabrication compatibility with mature manufacturing

technologies.[138] Optoelectronic devices require materials with specific intrinsic properties. High absorption coefficients and quantum efficiency ensure effective optoelectronic conversion at specific wavelengths. Materials with tunable bandgap allows precise and flexible control of optoelectronic properties. Low dark current upholds a high signal-to-noise ratio, minimizing interference for reliable information storage and processing. Additionally, the stability of materials maintains the performance and long-term reliability of optoelectronic devices. So far, precise control of wafer-scale growth and increasing synthesis yield are crucial challenges that need to be addressed. Additionally, process compatibility with mature technologies requires consideration of material physical properties such as, thermal expansion coefficient, lattice constant, and thermal conductivity. The integration of emerging materials requires a trade-off between performance metrics and commercial costs. In the future, wafer-scale candidate materials are required to transition from the lab to the factory and be integrated into industry-standard pilot lines. Driving the transition of single device toward large-scale functional circuits requires meeting the electronic-grade IC manufacturing requirements in accordance with the international roadmap for devices and systems (IRDS) standards for advanced technology nodes.

5.2. Device Design

Optoelectronic devices with high photoresponsivity, perception range, speed, energy efficiency, integration density, tunable plasticity, and multiple resistance states are ideal components for executing optoelectronic computing for visual processing. Optoelectronic devices can exhibit different figures of merits with different structures, including two terminals photodiode, three terminals phototransistors, and four terminals split gate. Two terminals photodiodes feature simple structure, making them highly compatible with 3D integration technology. Optoelectronic devices with multiple terminals exhibit high tunable plasticity through the gate modulation. Although various physical mechanisms of optoelectronic devices have been proposed, insufficient quantitative analysis and modeling still impede effective communication between IC manufacturers and designers. Compact models can forecast the behavior of optoelectronics, which assists designers in simulating the functionality of the systems and the process of device optimization. The lack of compact models that consider device performance in large-scale systems also hinders the optimization of relevant metrics.

5.3. Integration Technologies

The planar integration of processing units and readout circuits with optoelectronic devices inevitably limits the fill factor and affects the signal-to-noise ratio. An ideal strategy is to integrate these components in a monolithic-3D (M3D) configuration, where processing units and readout circuits can be designed beneath the optoelectronic devices. Compact interconnects contribute greatly to reducing parasitic resistance-capacitance delay and power consumption, while simultaneously increasing integration density. Thus, M3D integration holds the potential to achieve visual processing with high communication bandwidth. Silicon-based M3D integrated circuits are limited by the low thermal budget of CMOS backend-of-line integration. However, the 3D integration of emerging devices with a low thermal budget process presents a possible solution. Recent research has demonstrated wafer-level 3D integration based on MoS_2 and WSe_2 with more than 10 000 transistors per layer.[139] And the thermal budget is kept at a low level (180°C). Moreover, a low-temperature M3D integration method has been proposed through the dry lamination of prefabricated circuit layers tier by tier.[140] M3D-integrated 10 tiers of large-scale 2D transistors have been realized, with thermal budget lower than 120°C. Additionally, the carrier polarity in MoS_2 can be easily reconfigured from n-type to p-type via strong vdW interface coupling with antiferromagnetic insulator chromium oxychloride (CrOCl), thus constructing 3D complementary logic with a low thermal budget.[141] However, M3D integration still poses challenges in terms of high cost and reliability. Device performance degradation can result from fabrication conditions, such as high process temperatures during layer-by-layer integration, or from stacking-induced rough morphology. The enhanced thermal effects caused by compact interconnection in 3D stacked structures can generate noise and reduce accuracy, thus limiting computing performance. The interlayer dielectric also affects the electrostatic coupling in the M3D system. Therefore, further optimal strategies for contacts, interfaces, and gate dielectrics are necessary to achieve high-performance devices in M3D systems.

5.4. Algorithms

At the algorithm level, based on the combination of optoelectronic devices and neural network algorithms, the in-sensor computing can solve complex problems with simple hardware structures. One layer of the optoelectronic array is enough to enable number recognition and motion detection functionalities. Moreover, optoelectronic devices can exhibit nonlinear responsivity, which can be effectively utilized as a nonlinear operator. Most neural network architectures are based on linear operations, with nonlinear operators only as activation functions, which does not unlock the full potential of the network. Also, the nonlinear calculation in the conventional digital computing unit must be divided into several steps. This will consume more computational resources, and thus increase the power consumption and computation time. By incorporating nonlinear operations, in-sensor computing can achieve enhanced performance and fully exploit the capabilities of optoelectronics. A notable example is the recently proposed Kolmogorov-Arnold Networks,[142] which replace each weight parameter with a learnable 1D function in fully connected neural networks. With those nonlinear operations, the network has demonstrated up to 100-fold improvements in accuracy and efficiency. The nonlinear system requires the re-evaluation and redesign of neural network architectures from the perspectives of the device physics and characteristics.

Acknowledgements

Q.R. and C.Z. contributed equally to this work. This work was supported by MOST National Key Technologies R&D Programme

(No. SQ2022YFA1200118-04), Research Grant Council of Hong Kong (No. CRS_PolyU502/22). The Hong Kong Polytechnic University (Nos. 1-ZE1T and WZ4X), and The Hong Kong Polytechnic University Shenzhen Research Institute (No. I2022A013).

Conflict of Interest

The authors declare no conflict of interest.

Keywords

data compression, data structuring, in-sensor computing, optoelectronic devices, switching mechanisms

Received: May 26, 2024
Revised: June 27, 2024
Published online: July 14, 2024

[1] P. Bellini, P. Nesi, G. Pantaleo, *Appl. Sci.* **2022**, *12*, 1607.
[2] T. Wan, B. Shao, S. Ma, Y. Zhou, Q. Li, Y. Chai, *Adv. Mater.* **2023**, *35*, 2203830.
[3] J. Bryzek, *TSensors Summit*, December 8–9, Tokyo, Japan **2015**, pp. 1–63.
[4] Y. Liu, R. Fan, J. Guo, H. Ni, M. U. M. Bhutta, *Intell. Comput.* **2023**, *2*, 0043.
[5] R. Wang, S. Wang, K. Liang, Y. Xin, F. Li, Y. Cao, J. Lv, Q. Liang, Y. Peng, B. Zhu, *Small* **2022**, *18*, 2201111.
[6] S. W. Cho, C. Jo, Y. H. Kim, S. K. Park, *Nano-Micro Lett.* **2022**, *14*, 203.
[7] F. Zhou, J. Chen, X. Tao, X. Wang, Y. Chai, *Research* **2019**, *2019*, 9490413.
[8] S. Wang, X. Pan, L. Lyu, C. Y. Wang, P. Wang, C. Pan, Y. Yang, C. Wang, J. Shi, B. Cheng, *ACS Nano* **2022**, *16*, 4528.
[9] A. K. Jain, *Proc. IEEE* **1981**, *69*, 349.
[10] T. Wan, S. Ma, F. Liao, L. Fan, Y. Chai, *Sci. China Inform. Sci.* **2022**, *65*, 1.
[11] M. S. Kim, M. S. Kim, G. J. Lee, S. H. Sunwoo, S. Chang, Y. M. Song, D. H. Kim, *Adv. Mater. Technol.* **2022**, *7*, 2100144.
[12] V. J. Barranca, G. Kovačič, D. Zhou, D. Cai, *PLoS Comput. Biol.* **2014**, *10*, 1003793.
[13] Z. Wang, T. Wan, S. Ma, Y. Chai, *Nat. Nanotechnol.* **2024**, 1, https://doi.org/10.1038/s41565-024-01665-7.
[14] F. Zhong, Y. Chen, P. Yan, R. Li, Z. Ni, J. Lu, *Appl. Phys. Lett.* **2024**, *124*.
[15] M. Lefebvre, L. Moreau, R. Dekimpe, D. Bol, *IEEE Int. Solid-State Circ. Conf.* **2021**, *64*, 118
[16] Z. Sun, S. Kvatinsky, X. Si, A. Mehonic, Y. Cai, R. Huang, *Nat. Electron.* **2023**, *6*, 823.
[17] J. A. Mandelman, R. H. Dennard, G. B. Bronner, J. K. DeBrosse, R. Divakaruni, Y. Li, C. J. Radens, *IBM J. Res. Dev.* **2002**, *46*, 187.
[18] J. Zhang, W. Wang, J. Zhu, C. Wang, T. Zhu, C. Zhao, J. Wang, S. Zhang, X. Wang, K. C. Chang, *ACS Nano* **2024**, *18*, 3362.
[19] N. Youngblood, C. A. Ríos Ocampo, W. H. Pernice, H. Bhaskaran, *Nat. Photonics* **2023**, *17*, 561.
[20] J. Wu, M. Wei, J. Mu, H. Ma, C. Zhong, Y. Ye, C. Sun, B. Tang, L. Wang, J. Li, *ACS Nano* **2021**, *15*, 15982.
[21] J. Wu, H. Ma, C. Zhong, M. Wei, C. Sun, Y. Ye, Y. Xu, B. Tang, Y. Luo, B. Sun, *Nano Lett.* **2022**, *22*, 6816.
[22] R. Xu, S. Taheriniya, A. P. Ovvyan, J. R. Bankwitz, L. McRae, E. Jung, F. Brückerhoff-Plückelmann, I. Bente, F. Lenzini, H. Bhaskaran, *Opt. Mater. Express* **2023**, *13*, 3553.
[23] J. Feldmann, N. Youngblood, C. D. Wright, H. Bhaskaran, W. H. Pernice, *Nature* **2019**, *569*, 208.
[24] J. Wu, H. Ma, P. Yin, Y. Ge, Y. Zhang, L. Li, H. Zhang, H. Lin, *Small Sci.* **2021**, *1*, 2000053.
[25] B. Wu, H. Zhou, J. Dong, X. Zhang, *Appl. Phys. Rev.* **2024**, *11*, 011309.
[26] M. Wei, J. Li, Z. Chen, B. Tang, Z. Jia, P. Zhang, K. Lei, K. Xu, J. Wu, C. Zhong, *Adv. Photonics* **2023**, *5*, 046004.
[27] D. Oz, N. Suleymanov, B. Minkovich, V. Kostianovskii, L. Gantz, D. Polyushkin, T. Mueller, I. Goykhman, *ACS Photonics* **2023**, *10*, 1783.
[28] S. Abdollahramezani, O. Hemmatyar, M. Taghinejad, H. Taghinejad, A. Krasnok, A. A. Eftekhar, C. Teichrib, S. Deshmukh, M. A. El-Sayed, E. Pop, *Nat. Commun.* **2022**, *13*, 1696.
[29] H. Zhang, L. Zhou, L. Lu, J. Xu, N. Wang, H. Hu, B. A. Rahman, Z. Zhou, J. Chen, *ACS Photonics* **2019**, *6*, 2205.
[30] J. Feldmann, N. Youngblood, M. Karpov, H. Gehring, X. Li, M. Stappers, M. Le Gallo, X. Fu, A. Lukashchuk, A. S. Raja, *Nature* **2021**, *589*, 52.
[31] L. W. Luo, N. Ophir, C. P. Chen, L. H. Gabrielli, C. B. Poitras, K. Bergmen, M. Lipson, *Nat. Commun.* **2014**, *5*, 1.
[32] J. Wang, S. He, D. Dai, *Laser Photonics Rev.* **2014**, *8*, L18.
[33] Q. Xia, J. J. Yang, *Nat. Mater.* **2019**, *18*, 309.
[34] X. Pang, Y. Wang, Y. Zhu, Z. Zhang, D. Xiang, X. Ge, H. Wu, Y. Jiang, Z. Liu, X. Liu, *Nat. Commun.* **2024**, *15*, 1613.
[35] C. Y. Wang, S. J. Liang, S. Wang, P. Wang, Z. a. Li, Z. Wang, A. Gao, C. Pan, C. Liu, J. Liu, *Sci. Adv.* **2020**, *6*, eaba6173.
[36] Z. Zhang, S. Wang, C. Liu, R. Xie, W. Hu, P. Zhou, *Nat. Nanotechnol.* **2022**, *17*, 27.
[37] F. Zhou, Z. Zhou, J. Chen, T. H. Choy, J. Wang, N. Zhang, Z. Lin, S. Yu, J. Kang, H.-S. P. Wong, *Nat. Nanotechnol.* **2019**, *14*, 776.
[38] H. Seung, C. Choi, D. C. Kim, J. S. Kim, J. H. Kim, J. Kim, S. I. Park, J. A. Lim, J. Yang, M. K. Choi, *Sci. Adv.* **2022**, *8*, eabq3101.
[39] J. Chen, Z. Zhou, B. J. Kim, Y. Zhou, Z. Wang, T. Wan, J. Yan, J. Kang, J. H. Ahn, Y. Chai, *Nat. Nanotechnol.* **2023**, *18*, 882.
[40] Q. B. Zhu, B. Li, D. D. Yang, C. Liu, S. Feng, M. L. Chen, Y. Sun, Y. N. Tian, X. Su, X. M. Wang, *Nat. Commun.* **2021**, *12*, 1798.
[41] Y. Zhou, J. Fu, Z. Chen, F. Zhuge, Y. Wang, J. Yan, S. Ma, L. Xu, H. Yuan, M. Chan, *Nat. Electron.* **2023**, *6*, 870.
[42] Y. Zhou, J. Fu, T. Wan, L. Xu, S. Ma, J. Chen, X. Miao, Y. He, Y. Chai, *2022 International Electron Devices Meeting (IEDM)*, IEEE, New York **2022**, p. 31.4.1-31.4.4.
[43] G. Chen, H. Cao, J. Conradt, H. Tang, F. Rohrbein, A. Knoll, *IEEE Signal Proc. Mag.* **2020**, *37*, 34.
[44] F. Liao, F. Zhou, Y. Chai, *J. Semicond.* **2021**, *42*, 013105.
[45] P. Lichtsteiner, C. Posch, T. Delbruck, *IEEE J. Solid-St. Circ.* **2008**, *43*, 566.
[46] J. A. Leñero-Bardallo, T. Serrano-Gotarredona, B. Linares-Barranco, *IEEE J. Solid-St. Circ.* **2011**, *46*, 1443.
[47] A. Armin, R. D. Jansen-van Vuuren, N. Kopidakis, P. L. Burn, P. Meredith, *Nat. Commun.* **2015**, *6*, 6343.
[48] Q. Liu, S. Zeiske, X. Jiang, D. Desta, S. Mertens, S. Gielen, R. Shanivarasanthe, H. G. Boyen, A. Armin, K. Vandewal, *Nat. Commun.* **2022**, *13*, 5194.
[49] B. Siegmund, A. Mischok, J. Benduhn, O. Zeika, S. Ullbrich, F. Nehm, M. Böhm, D. Spoltore, H. Fröb, C. Körner, *Nat. Commun.* **2017**, *8*, 15421.
[50] C. Jo, J. Kim, J. Y. Kwak, S. M. Kwon, J. B. Park, J. Kim, G. S. Park, M. G. Kim, Y. H. Kim, S. K. Park, *Adv. Mater.* **2022**, *34*, 2108979.
[51] H. S. Rao, W. G. Li, B. X. Chen, D. B. Kuang, C. Y. Su, *Adv. Mater.* **2017**, *29*, 1602639.
[52] M. I. Saidaminov, M. A. Haque, M. Savoie, A. L. Abdelhady, N. Cho, I. Dursun, U. Buttner, E. Alarousu, T. Wu, O. M. Bakr, *Adv. Mater.* **2016**, *28*, 8144.
[53] J. Wang, S. Xiao, W. Qian, K. Zhang, J. Yu, X. Xu, G. Wang, S. Zheng, S. Yang, *Adv. Mater.* **2021**, *33*, 2005557.

[54] F. Cao, J. Chen, D. Yu, S. Wang, X. Xu, J. Liu, Z. Han, B. Huang, Y. Gu, K. L. Choy, *Adv. Mater.* **2020**, *32*, 1905362.
[55] L. Pi, P. Wang, S. J. Liang, P. Luo, H. Wang, D. Li, Z. Li, P. Chen, X. Zhou, F. Miao, *Nat. Electron.* **2022**, *5*, 248.
[56] W. T. Chen, A. Y. Zhu, V. Sanjeev, M. Khorasaninejad, Z. Shi, E. Lee, F. Capasso, *Nat. Nanotechnol.* **2018**, *13*, 220.
[57] W. Xin, W. Zhong, Y. Shi, Y. Shi, J. Jing, T. Xu, J. Guo, W. Liu, Y. Li, Z. Liang, *Adv. Mater.* **2024**, *36*, 2306772.
[58] F. Wang, S. Zhu, W. Chen, J. Han, R. Duan, C. Wang, M. Dai, F. Sun, Y. Jin, Q. J. Wang, *Nat. Nanotechnol.* **2024**, *19*, 455.
[59] H. Yuan, X. Liu, F. Afshinmanesh, W. Li, G. Xu, J. Sun, B. Lian, A. G. Curto, G. Ye, Y. Hikita, *Nat. Nanotechnol.* **2015**, *10*, 707.
[60] L. Tong, X. Huang, P. Wang, L. Ye, M. Peng, L. An, Q. Sun, Y. Zhang, G. Yang, Z. Li, *Nat. Commun.* **2020**, *11*, 2308.
[61] S. Chen, R. Cao, X. Chen, Q. Wu, Y. Zeng, S. Gao, Z. Guo, J. Zhao, M. Zhang, H. Zhang, *Adv. Mater. Interfaces* **2020**, *7*, 1902179.
[62] S. D. Namgung, R. M. Kim, Y. C. Lim, J. W. Lee, N. H. Cho, H. Kim, J. S. Huh, H. Rhee, S. Nah, M. K. Song, *Nat. Commun.* **2022**, *13*, 5081.
[63] J. Wei, C. Xu, B. Dong, C. W. Qiu, C. Lee, *Nat. Photonics* **2021**, *15*, 614.
[64] H. Ren, G. Briere, X. Fang, P. Ni, R. Sawant, S. Héron, S. Chenot, S. Vézian, B. Damilano, V. Brändli, *Nat. Commun.* **2019**, *10*, 2986.
[65] A. Arbabi, Y. Horie, M. Bagheri, A. Faraon, *Nat. Nanotechnol.* **2015**, *10*, 937.
[66] A. J. Molina-Mendoza, M. Paur, T. Mueller, *Adv. Opt. Mater.* **2020**, *8*, 2000417.
[67] L. Mennel, J. Symonowicz, S. Wachter, D. K. Polyushkin, A. J. Molina-Mendoza, T. Mueller, *Nature* **2020**, *579*, 62.
[68] X. Pan, J. Shi, P. Wang, S. Wang, C. Pan, W. Yu, B. Cheng, S. J. Liang, F. Miao, *Sci. Adv.* **2023**, *9*, eadi4083.
[69] J. Y. Chen, C. W. Huang, C. H. Chiu, Y. T. Huang, W. W. Wu, *Adv. Mater.* **2015**, *27*, 5028.
[70] Z. Wang, H. Wu, G. W. Burr, C. S. Hwang, K. L. Wang, Q. Xia, J. J. Yang, *Nat. Rev. Mater.* **2020**, *5*, 173.
[71] W. Huh, D. Lee, C. H. Lee, *Adv. Mater.* **2020**, *32*, 2002092.
[72] J. J. Yang, M. D. Pickett, X. Li, D. A. Ohlberg, D. R. Stewart, R. S. Williams, *Nat. Nanotechnol.* **2008**, *3*, 429.
[73] Y. Wang, J. Yang, Z. Wang, J. Chen, Q. Yang, Z. Lv, Y. Zhou, Y. Zhai, Z. Li, S. T. Han, *Small* **2019**, *15*, 1805431.
[74] T. Y. Wang, J. L. Meng, Q. X. Li, Z. Y. He, H. Zhu, L. Ji, Q. Q. Sun, L. Chen, D. W. Zhang, *Nano Energy* **2021**, *89*, 106291.
[75] D. W. DeQuilettes, W. Zhang, V. M. Burlakov, D. J. Graham, T. Leijtens, A. Osherov, V. Bulović, H. J. Snaith, D. S. Ginger, S. D. Stranks, *Nat. Commun.* **2016**, *7*, 11683.
[76] P. Löper, M. Stuckelberger, B. Niesen, J. Werner, M. Filipič, S. J. Moon, J. H. Yum, M. Topič, S. De Wolf, C. Ballif, *J. Phys. Chem. Lett.* **2015**, *6*, 66.
[77] X. Zhu, J. Lee, W. D. Lu, *Adv. Mater.* **2017**, *29*, 1700527.
[78] Y. Wang, Z. Lv, Q. Liao, H. Shan, J. Chen, Y. Zhou, L. Zhou, X. Chen, V. A. Roy, Z. Wang, *Adv. Mater.* **2018**, *30*, 1800327.
[79] T. Tsujioka, Y. Hamada, K. Shibata, A. Taniguchi, T. Fuyuki, *Appl. Phys. Lett.* **2001**, *78*, 2282.
[80] J. Zhang, Q. Zou, H. Tian, *Adv. Mater.* **2013**, *25*, 378.
[81] Y. Wang, B. Han, M. Mayor, P. Samorì, *Adv. Mater.* **2024**, *36*, 2307359.
[82] T. Leydecker, M. Herder, E. Pavlica, G. Bratina, S. Hecht, E. Orgiu, P. Samorì, *Nat. Nanotechnol.* **2016**, *11*, 769.
[83] L. Hou, X. Zhang, G. F. Cotella, G. Carnicella, M. Herder, B. M. Schmidt, M. Pätzel, S. Hecht, F. Cacialli, P. Samorì, *Nat. Nanotechnol.* **2019**, *14*, 347.
[84] M. E. Gemayel, K. Börjesson, M. Herder, D. T. Duong, J. A. Hutchison, C. Ruzié, G. Schweicher, A. Salleo, Y. Geerts, S. Hecht, *Nat. Commun.* **2015**, *6*, 6330.
[85] S. Wall, S. Yang, L. Vidas, M. Chollet, J. M. Glownia, M. Kozina, T. Katayama, T. Henighan, M. Jiang, T. A. Miller, *Science* **2018**, *362*, 572.
[86] J. Del Valle, N. M. Vargas, R. Rocco, P. Salev, Y. Kalcheim, P. N. Lapa, C. Adda, M. H. Lee, P. Y. Wang, L. Fratino, *Science* **2021**, *373*, 907.
[87] Y. C. Lin, D. O. Dumcenco, Y. S. Huang, K. Suenaga, *Nat. Nanotechnol.* **2014**, *9*, 391.
[88] G. Gao, Y. Jiao, F. Ma, Y. Jiao, E. Waclawik, A. Du, *J. Phys. Chem. C* **2015**, *119*, 13124.
[89] C. Ríos, M. Stegmaier, P. Hosseini, D. Wang, T. Scherer, C. D. Wright, H. Bhaskaran, W. H. Pernice, *Nat. Photonics* **2015**, *9*, 725.
[90] G. Li, D. Xie, Z. Zhang, Q. Zhou, H. Zhong, H. Ni, J. Wang, E. j. Guo, M. He, C. Wang, *Adv. Funct. Mater.* **2022**, *32*, 2203074.
[91] G. Li, D. Xie, H. Zhong, Z. Zhang, X. Fu, Q. Zhou, Q. Li, H. Ni, J. Wang, E.-j. Guo, *Nat. Commun.* **2022**, *13*, 1729.
[92] K. Chang, X. Zhao, X. Yu, Z. Gan, R. Wang, A. Dong, Z. Zhao, Y. Zhang, H. Wang, *Nano Lett.* **2023**, *23*, 8288.
[93] N. Farmakidis, N. Youngblood, X. Li, J. Tan, J. L. Swett, Z. Cheng, C. D. Wright, W. H. Pernice, H. Bhaskaran, *Sci. Adv.* **2019**, *5*, eaaw2687.
[94] Y. Y. Au, H. Bhaskaran, C. D. Wright, *Sci. Rep.* **2017**, *7*, 9688.
[95] I. Grinberg, D. V. West, M. Torres, G. Gou, D. M. Stein, L. Wu, G. Chen, E. M. Gallo, A. R. Akbashev, P. K. Davies, J. E. Spanier, A. M. Rappe, *Nature* **2013**, *503*, 509.
[96] M. Nakamura, S. Horiuchi, F. Kagawa, N. Ogawa, T. Kurumaji, Y. Tokura, M. Kawasaki, *Nat. Commun.* **2017**, *8*, 281.
[97] B. I. Sturman, *Physics* **2020**, *63*, 407.
[98] M.-M. Yang, Z.-D. Luo, D. J. Kim, M. Alexe, *Appl. Phys. Lett.* **2017**, *110*, 183902.
[99] M. M. Yang, M. Alexe, *Adv. Mater.* **2018**, *30*, 1704908.
[100] X. Long, H. Tan, F. Sanchez, I. Fina, J. Fontcuberta, *Nat. Commun.* **2021**, *12*, 382.
[101] T. Li, A. Lipatov, H. Lu, H. Lee, J. W. Lee, E. Torun, L. Wirtz, C. B. Eom, J. Iniguez, A. Sinitskii, A. Gruverman, *Nat. Commun.* **2018**, *9*, 3344.
[102] Q. Yang, J. Cao, Y. Zhou, L. Sun, X. Lou, *Acta Mater.* **2016**, *112*, 216.
[103] Y. Wang, M. K. Niranjan, K. Janicka, J. P. Velev, M. Y. Zhuravlev, S. S. Jaswal, E. Y. Tsymbal, *Phys. Rev. B.* **2010**, *82*, 094114.
[104] C.-G. Duan, R. F. Sabirianov, W.-N. Mei, S. S. Jaswal, E. Y. Tsymbal, *Nano Lett.* **2006**, *6*, 483.
[105] F. Xue, X. He, W. Liu, D. Periyanagounder, C. Zhang, M. Chen, C. H. Lin, L. Luo, E. Yengel, V. Tung, *Adv. Funct. Mater.* **2020**, *30*, 2004206.
[106] K. Xu, W. Jiang, X. Gao, Z. Zhao, T. Low, W. Zhu, *Nanoscale* **2020**, *12*, 23488.
[107] A. V. Kimel, M. Li, *Nat. Rev. Mater.* **2019**, *4*, 189.
[108] N. Fang, C. Wu, Y. Zhang, Z. Li, Z. Zhou, *ACS Nano* **2024**, *18*, 8600.
[109] C. D. Stanciu, F. Hansteen, A. V. Kimel, A. Kirilyuk, A. Tsukamoto, A. Itoh, T. Rasing, *Phys. Rev. Lett.* **2007**, *99*, 047601.
[110] C. H. Lambert, S. Mangin, B. C. S. Varaprasad, Y. Takahashi, M. Hehn, M. Cinchetti, G. Malinowski, K. Hono, Y. Fainman, M. Aeschlimann, *Science* **2014**, *345*, 1337.
[111] S. Mangin, M. Gottwald, C. Lambert, D. Steil, V. Uhlíř, L. Pang, M. Hehn, S. Alebrand, M. Cinchetti, G. Malinowski, *Nat. Mater.* **2014**, *13*, 286.
[112] J. Y. Chen, L. He, J. P. Wang, M. Li, *Phys. Rev. Appl.* **2017**, *7*, 021001.
[113] P. Zhang, T. F. Chung, Q. Li, S. Wang, Q. Wang, W. L. Huey, S. Yang, J. E. Goldberger, J. Yao, X. Zhang, *Nat. Mater.* **2022**, *21*, 1373.
[114] X. Wang, C. Xiao, H. Park, J. Zhu, C. Wang, T. Taniguchi, K. Watanabe, J. Yan, D. Xiao, D. R. Gamelin, *Nature* **2022**, *604*, 468.
[115] O. H.-C. Cheng, D. H. Son, M. Sheldon, *Nat. Photonics* **2020**, *14*, 365.
[116] W. Guo, M. E. Fouda, A. M. Eltawil, K. N. Salama, *Front. Neurosci.* **2021**, *15*, 638474.
[117] J. Wang, Z. Lv, X. Xing, X. Li, Y. Wang, M. Chen, G. Pang, F. Qian, Y. Zhou, S. T. Han, *Adv. Funct. Mater.* **2020**, *30*, 1909114.

[118] Y. Pei, L. Yan, Z. Wu, J. Lu, J. Zhao, J. Chen, Q. Liu, X. Yan, *ACS Nano* **2021**, *15*, 17319.
[119] R. Yuan, P. J. Tiw, L. Cai, Z. Yang, C. Liu, T. Zhang, C. Ge, R. Huang, Y. Yang, *Nat. Commun.* **2023**, *14*, 3695.
[120] R. Yuan, Q. Duan, P. J. Tiw, G. Li, Z. Xiao, Z. Jing, K. Yang, C. Liu, C. Ge, R. Huang, *Nat. Commun.* **2022**, *13*, 3973.
[121] J. Lee, S. Pak, Y.-W. Lee, Y. Cho, J. Hong, P. Giraud, H. S. Shin, S. M. Morris, J. I. Sohn, S. Cha, *Nat. Commun.* **2017**, *8*, 14734.
[122] F. Liao, Z. Zhou, B. J. Kim, J. Chen, J. Wang, T. Wan, Y. Zhou, A. T. Hoang, C. Wang, J. Kang, *Nat. Electron.* **2022**, *5*, 84.
[123] Y. Hu, M. Dai, W. Feng, X. Zhang, S. Zhang, B. Tan, H. Shang, Y. Q. Fu, P. Hu, *Mater. Horiz.* **2020**, *7*, 3316.
[124] T. S. Jensen, N. B. Finnerup, *Lancet Neurol.* **2014**, *13*, 924.
[125] S. Ke, Y. He, L. Zhu, Z. Jiang, H. Mao, Y. Zhu, C. Wan, Q. Wan, *Adv. Electron. Mater.* **2021**, *7*, 2100487.
[126] M. Kumar, H. S. Kim, J. Kim, *Adv. Mater.* **2019**, *31*, 1900021.
[127] H. Zhang, P. Qiu, Y. Lu, X. Ju, D. Chi, K. S. Yew, M. Zhu, S. Wang, R. Wei, W. Hu, *ACS Sens.* **2023**, *8*, 3873.
[128] M. K. Kim, J. S. Lee, *Adv. Mater.* **2020**, *32*, 1907826.
[129] T. Ohshiro, D. E. Angelaki, G. C. DeAngelis, *Nat. Neurosci.* **2011**, *14*, 775.
[130] S. Ma, Y. Zhou, T. Wan, Q. Ren, J. Yan, L. Fan, H. Yuan, M. Chan, Y. Chai, *Nano Lett.* **2024**, *24*, 7091.
[131] M. U. K. Sadaf, N. U. Sakib, A. Pannone, H. Ravichandran, S. Das, *Nat. Commun.* **2023**, *14*, 5729.
[132] X. Wu, E. Li, Y. Liu, W. Lin, R. Yu, G. Chen, Y. Hu, H. Chen, T. Guo, *Nano Energy* **2021**, *85*, 106000.
[133] J. You, L. Wang, Y. Zhang, D. Lin, B. Wang, Z. Han, N. Zhang, T. Miao, M. Liu, Z. Jiang, *Nano Res.* **2023**, *16*, 7405.
[134] J. Yu, X. Yang, G. Gao, Y. Xiong, Y. Wang, J. Han, Y. Chen, H. Zhang, Q. Sun, Z. L. Wang, *Sci. Adv.* **2021**, *7*, eabd9117.
[135] J. Zha, Y. Xia, S. Shi, H. Huang, S. Li, C. Qian, H. Wang, P. Yang, Z. Zhang, Y. Meng, *Adv. Mater.* **2024**, *36*, 2308502.
[136] K. Liu, T. Zhang, B. Dang, L. Bao, L. Xu, C. Cheng, Z. Yang, R. Huang, Y. Yang, *Nat. Electron.* **2022**, *5*, 761.
[137] Y. Zheng, S. Ghosh, S. Das, *Adv. Mater.* **2023**, 2307380.
[138] Y. Xia, X. Chen, J. Wei, S. Wang, S. Chen, S. Wu, M. Ji, Z. Sun, Z. Xu, W. Bao, *Nat. Mater.* **2023**, *22*, 1324.
[139] D. Jayachandran, R. Pendurthi, M. U. K. Sadaf, N. U. Sakib, A. Pannone, C. Chen, Y. Han, N. Trainor, S. Kumari, T. V. Mc Knight, *Nature* **2024**, *625*, 276.
[140] D. Lu, Y. Chen, Z. Lu, L. Ma, Q. Tao, Z. Li, L. Kong, L. Liu, X. Yang, S. Ding, X. Liu, Y. Li, R. Wu, Y. Wang, Y. Hu, X. Duan, L. Liao, Y. Liu, *Nature* **2024**, *630*, 340.
[141] Y. Guo, J. Li, X. Zhan, C. Wang, M. Li, B. Zhang, Z. Wang, Y. Liu, K. Yang, H. Wang, *Nature* **2024**, *630*, 346.
[142] Z. Liu, Y. Wang, S. Vaidya, F. Ruehle, J. Halverson, M. Soljačić, T. Y. Hou, M. Tegmark, preprint arXiv:2404.19756 **2024**.